Experimental demonstration of the validity of the quantum heat-exchange fluctuation relation in an NMR setup

Soham Pal,[*] T. S. Mahesh,[†] and Bijay Kumar Agarwalla [‡]

Department of Physics, Indian Institute of Science Education and Research, Pune 411008, India

We experimentally explore the validity of the Jarzynski and Wójcik quantum heat-exchange fluctuation relation by implementing an interferometric technique in liquid-state nuclear magnetic resonance setup and study the heat-exchange statistics between two coupled spin-1/2 quantum systems. We experimentally emulate two models—(i) the *XY*-coupling model, containing an energy conserving interaction between the qubits, and (ii) the *XX*-coupling model—and analyze the regimes of validity and violation of the fluctuation symmetry when the composite system is prepared in an uncorrelated initial state with individual spins prepared in local Gibbs thermal states at different temperatures. We further extend our analysis for heat exchange by incorporating correlation in the initial state. We support our experimental findings by providing exact analytical results. Our experimental approach is general and can be systematically extended to study heat statistics for more complex out-of-equilibrium many-body quantum systems.

I. INTRODUCTION

Quantifying thermal and quantum fluctuations for mesoscopic and nanoscale systems are important from both fundamental and practical perspectives [1]. In the past two decades, considerable research has been devoted to developing a consistent theoretical framework to describe these fluctuations, which have led to the discovery of what are now collectively referred to as "fluctuation relations" [2–18]. For out-of-equilibrium systems, classical or quantum, various thermodynamic observables such as work and heat are found to follow these universal relations in transient [5–7] and/or in steady-state regimes [16,17]. Apart from quantifying the probability of observing the rare events related to negative entropy production, fluctuation relations correctly describe systems residing arbitrarily far from equilibrium and further serve as an essential ingredient for establishing the rapidly growing field of quantum thermodynamics [19–21].

Despite impressive theoretical progress, experimental verification of these fluctuation relations remained a challenge in the quantum domain, primarily because of the requirement of projective measurements to construct the probability distribution function (PDF) for work and heat. Recently, several experimental proposals have been put forward to construct such PDFs [22–28]. Following a projective measurement scheme, the first experimental success for the work fluctuation relation was achieved in an ion-trap setup [29–32]. Later, this difficult projective measurement scheme was circumvented and an ancilla-based Ramsey interferometric approach was proposed [23], following which the work fluctuation relation was verified [24,25]. Further successful attempts were also

made recently to study similar fluctuation relations for open systems [32].

In this work, we attempt to explore the validity of the quantum version of Jarzynski and Wójcik's heat-*exchange fluctuation theorem* (XFT) [7]. We employ here a similar interferometric approach, as proposed for measuring work statistics, in a liquid nuclear magnetic resonance (NMR) architecture to extract the full statistics of heat, flowing between two coherent quantum systems, by reading out the ancilla. We test the XFT for an uncorrelated (product) initial state for an arbitrary transient time for two setups: (i) the *XY*-coupling model and (ii) the *XX*-coupling model. Interestingly, for the first model the XFT is satisfied for arbitrary coupling strength, whereas for the second model the XFT is satisfied only in the weak-coupling limit, as originally proposed by Jarzynski and Wójcik. We further investigate another possible regime for the violation of XFT by incorporating a correlated initial state and observe an apparent spontaneous heat flow from cold to hot.

The paper is organized as follows. In Sec. II, we briefly sketch the proof of the heat-exchange fluctuation relation following a two-point measurement scheme and highlight the key approximations under which this relation is protected. In Sec. III, we present our experimental setup along with the NMR interferometric technique and discuss how to extract the heat statistics. In Secs. IV and V, we present our results for the *XY* and *XX* models. Finally, we conclude and discuss the future directions in Sec. VI. Certain details about the experimental techniques are provided in the Appendixes.

II. HEAT STATISTICS AND EXCHANGE FLUCTUATION RELATION IN THE QUANTUM DOMAIN

Here we give a brief summary of the heat statistics formalism and the corresponding Jarzynski and Wójcik XFT. We consider two quantum systems (system 1 and system 2) described by Hamiltonians H_1 and H_2 that are initially

———————

[*]soham.pal@students.iiserpune.ac.in
[†]mahesh.ts@iiserpune.ac.in
[‡]bijay@iiserpune.ac.in

$(t = 0^-)$ decoupled and separately equilibrated at different inverse temperatures, β_1 and β_2, respectively. The composite system initially resides in an uncorrelated state $\rho_0 = \rho_1 \otimes \rho_2$, with $\rho_i = \exp[-\beta_i H_i]/Z_i$, $i = 1, 2$, being the Gibbs thermal state and $Z_i = \text{Tr}[\exp[-\beta_i H_i]]$ being the corresponding partition function. At $t = 0$, a constant coupling between the two systems is suddenly switched on, which allows finite heat exchange for a duration $t = \tau$, after which the interaction is suddenly turned off. This exchanged heat is a stochastic variable due to the inherent nondeterministic nature of quantum evolution and the randomness in the initial state preparation. To quantify the associated PDF and to further connect with the XFT, we follow a two-time projective measurement scheme [12,13,33], one at the beginning and the other at the end of the heat-exchange process. We first consider the joint PDF for energy change (ΔE_i) for both systems, given as

$$p_\tau(\Delta E_1, \Delta E_2) = \sum_{m,n} \left\{ \prod_{i=1}^{2} \delta\left[\Delta E_i - \left(\epsilon_m^i - \epsilon_n^i\right)\right] \right\} p_{m|n}^\tau p_n^0,$$

(1)

where $p_n^0 = \prod_{i=1}^{2} e^{-\beta_i \epsilon_n^i}/Z_i$ is the probability of finding the system in the common eigenstate $|n\rangle$ with energy eigenvalue ϵ_n^i after the first projective measurement. The second projective measurement, at $t = \tau$, collapses the system into another common eigenstate $|m\rangle$ with probability $p_{m|n}^\tau = |\langle m|\mathcal{U}(\tau, 0)|n\rangle|^2$, where $\mathcal{U}(t, 0) = e^{-\frac{i}{\hbar}\mathcal{H}t}$ represents the unitary propagator evolving with the composite Hamiltonian $\mathcal{H}$. Now using the principle of microreversibility of quantum dynamics for the autonomous system $p_{m|n}^\tau = p_{n|m}^\tau$ and with the given uncorrelated Gibbs initial condition, one obtains

$$p_\tau(\Delta E_1, \Delta E_2) = e^{\beta_1 \Delta E_1 + \beta_2 \Delta E_2} p_\tau(-\Delta E_1, -\Delta E_2).$$
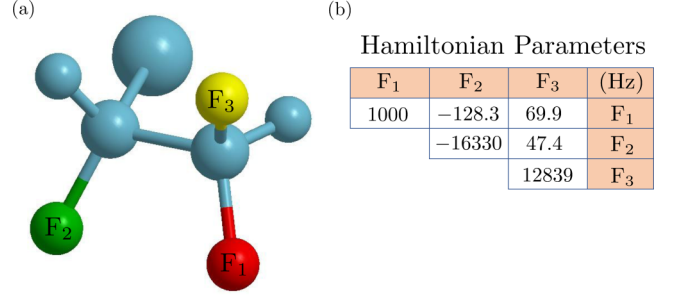
(2)

At the limit where the interaction energy between the two systems is small in comparison to the internal energy of each system, i.e., in the *weak*-coupling limit, ΔE_1 and ΔE_2 can be interpreted as heat, and by defining $\Delta E_1 \approx -\Delta E_2 = Q$, one arrives at the Jarzynski and Wójcik XFT, given as [12,34]

$$p_\tau(Q) = \exp[(\beta_1 - \beta_2)Q]p_\tau(-Q).$$

(3)

Equation (3) also implies that $\langle e^{-\Delta\beta Q}\rangle_\tau = 1$, where $\langle\ldots\rangle_\tau$ represents the average performed over the distribution $p_\tau(Q)$ and $\Delta\beta = \beta_1 - \beta_2$. In this work, our primary quantity of interest is the corresponding characteristic function (CF), given by the Fourier transformation of the heat PDF $p_\tau(Q)$ [34],

$$\chi_\tau(u) = \int dQ\, e^{-iuQ}\, p_\tau(Q),$$
$$= \text{Tr}[\mathcal{U}^\dagger(\tau, 0)(e^{-iuH_1} \otimes 1_2)\mathcal{U}(\tau, 0)(e^{iuH_1} \otimes 1_2)\rho_0].$$

(4)

Here u is the parameter conjugate to Q. For the CF, the XFT in Eq. (3) translates to $\chi_\tau(u) = \chi_\tau(-u - i(\beta_1 - \beta_2))$ [35–38]. In what follows, we implement experimentally the ancilla-assisted interferometric scheme in liquid NMR architecture to measure the above CF and extract the corresponding heat PDF [26–28] to analyze the heat-exchange process and the corresponding XFT. Interestingly, the ancilla-based technique also offers analysis of the CF for arbitrary initial preparation, which includes quantum correlations and quantum coherences

of the the composite system (see Appendix A). The CF obtained following the projective measurement scheme fails to capture signatures that arise from such correlated initial states.

1, 1, 2–Trifluoro –2 –iodoethane

FIG. 1. (a) Structure of the molecule used in the experiments: 1,1,2-trifluoro-2-iodoethane. We identify F_3 as the ancilla qubit and the heat exchange takes place between F_1 and F_2. (b) Table listing the parameters of the Hamiltonian in Eq. (5). Diagonal terms represent the nuclear offset frequencies ν_i and off-diagonal terms represent the scalar coupling J_{ij}.

III. EXPERIMENTAL SETUP AND INTERFEROMETRIC TECHNIQUE

In our experiments, we use liquid-state NMR spectroscopy of three ^{19}F nuclei (F_1, F_2, and F_3) in 1,1,2-trifluoro-2-iodoethane (TFIE) (Fig. 1), dissolved in acetone. All our experiments are performed in a 500-MHz Bruker NMR spectrometer at an ambient temperature. We identify F_1 as qubit 1, F_2 as qubit 2, and F_3 as the ancillary qubit. The molecules in the sample are all identical and sufficiently isolated [39–41] and all the dynamics and heat-exchange processes are completed on the time scale of milliseconds, such that any relevant environmental effects can be neglected. Note that the longitudinal and transverse relaxation time constants in our NMR setup are in fact of the order of few seconds. The internal Hamiltonian (H_{int}) of the three-spin system in the rotating frame of radio-frequency (RF) pulses can be written as (see Appendix C for details)

$$H_{\text{int}} = \sum_{i=1}^{3} \frac{h\nu_i}{2}\sigma_i^z + \sum_{i<j=1}^{3} \frac{hJ_{ij}}{4}\sigma_i^z\sigma_j^z,$$

(5)

where ν_i is the offset frequency of the ith nucleus and J_{ij} is the scalar coupling between the ith and the jth nuclei as explained in Fig. 1. F_1 and F_2 exchange heat by interacting under a constant-coupling Hamiltonian. Here we consider two models to study the heat exchange and corresponding XFT. The first composite Hamiltonian for F_1 and F_2 that we simulate in our experiment is given as

$$\mathcal{H} = H_1 + H_2 + \frac{hJ}{4}\left(\sigma_1^x \otimes \sigma_2^y - \sigma_1^y \otimes \sigma_2^x\right),$$

(6)

which we refer to here as the *XY* model. The other model, referred to as the *XX* model, is given by

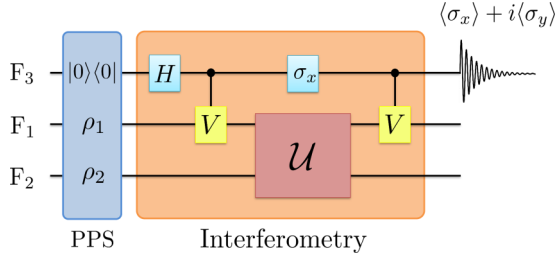$$\mathcal{H} = H_1 + H_2 + \frac{hJ}{4}\sigma_1^x \otimes \sigma_2^x,$$

(7)

FIG. 2. Circuit diagram for the interferometric technique to measure the characteristic function of heat, $\chi_\tau(u)$. Here, H is the Hadamard gate applied on the ancillary qubit, initially prepared in the pseudo pure state $|0\rangle\langle 0|$, followed by a control gate $V = \exp[-iuH_1] \otimes \mathbb{1}_2$ on the qubit F_1. Here $\mathcal{U} = \exp[-\frac{i}{\hbar}\mathcal{H}\tau]$ is the unitary propagator where $\mathcal{H}$ represents the Hamiltonian of the composite system involving the qubits F_1 and F_2. In our study, $\mathcal{H}$ corresponds to either the XY-model Eq. (6) or the XX-model Eq. (7). ρ_1, ρ_2 are the initial states of F_1 and F_2, respectively. The readout of the combination $\langle \sigma_x \rangle + i\langle \sigma_y \rangle$ of the ancilla hands over the characteristic function $\chi_\tau(u)$.

where $H_1 = \frac{-h\nu_0}{2}\sigma_1^z \otimes \mathbb{1}_2$, and $H_2 = \mathbb{1}_1 \otimes \frac{-h\nu_0}{2}\sigma_2^z$. $\sigma^i (i = x, y, z)$ is the ith component of the Pauli spin-1/2 operator. Recall that we are interested in extracting the statistics of heat flowing between qubit F_1 and qubit F_2 by measuring the CF, $\chi_\tau(u)$ as given in Eq. (4). For the first set of experiments for both these models we consider an uncorrelated (product) initial state for the qubits. By taking advantage of the spatial averaging technique [42] (see Appendix B), we prepare the ancillary qubit (F_3) in a pseudopure state $|0\rangle\langle 0|$ and the other two qubits of ^{19}F nuclei (F_1 and F_2) in a pseudoequilibrium state $\rho_1 \otimes \rho_2$, where $\rho_i = \exp[-\beta_i H_i]/\mathcal{Z}_i$ is the Gibbs thermal state with inverse pseudospin temperatures β_i. In our experiments, we realize different pseudospin temperatures by applying RF pulses from 0 to $\pi/2$ that redistribute the population between the qubit states, followed by a pulsed field gradient (PFG) which destroys the coherences and produces the desired thermal initial state. Note that the pseudospin temperature is different from the actual sample temperature, which is always maintained at an ambient temperature.

Following the above initialization procedure, we incorporate an interferometric protocol [24,25], shown in Fig. 2, which maps the $\chi_\tau(u)$ onto the ancillary qubit F_3. Various gates used for this protocol such as the Hadamard gate H, the controlled gate $V = \exp[-iuH_1] \otimes \mathbb{1}_2$, and the unitary operator $\mathcal{U} = \exp[-\frac{i}{\hbar}\mathcal{H}\tau]$, responsible for heat exchange between the qubits, are prepared by utilizing the internal Hamiltonian H_{int} [Eq. (5)] and the RF pulses. The corresponding experimental pulse sequences are presented in Appendix B. At the end of this entire protocol, the desired CF $\chi_\tau(u)$ is obtained by reading out the $\langle \sigma_x \rangle$ and $\langle \sigma_y \rangle$ components of the ancilla (see Appendix A) and the inverse Fourier transform of the combination $\langle \sigma_x \rangle + i\langle \sigma_y \rangle$ then provides the desired PDF $p_\tau(Q)$.

IV. RESULTS AND DISCUSSION

A. *XY*-coupling model

We first present experimental results for the XY model. For this particular model, we set the frequency for qubits F_1 and
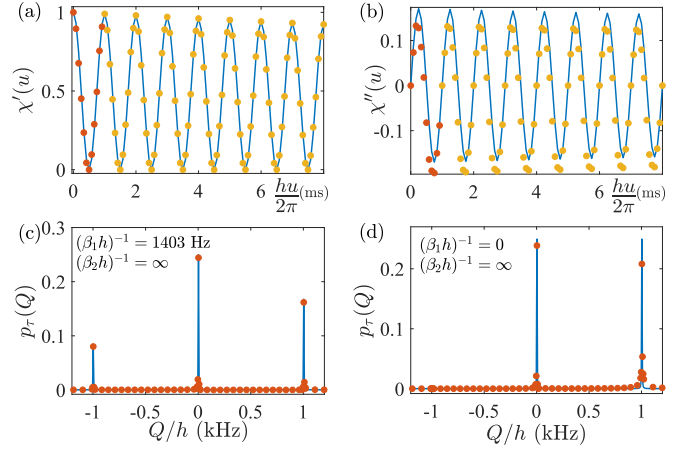

FIG. 3. Results for the XY model. (a, b) Plots of the real [$\chi_\tau'(u)$] and imaginary [$\chi_\tau''(u)$] components of the CF $\chi_\tau(u)$ for $\nu_0 = 1$ kHz and $J = 1$ Hz at $(\beta_1 h)^{-1} = 1403$ Hz and $(\beta_2 h)^{-1} = \infty$. The duration of heat exchange is $\tau = \pi/J$. Solid blue lines and dots correspond to theoretical and experimental results, respectively. Red dots represent the set of experimental data taken in one complete period ($u = \frac{2\pi}{h\nu_0}$) and orange dots represent extrapolated data points. (c, d) PDF of heat exchange $p_\tau(Q)$ for $(\beta_1 h)^{-1} = 1403$ Hz and $(\beta_1 h)^{-1} = 0$, respectively.

F_2 as $\nu_0 = 1$ kHz and the coupling J is chosen as 1 Hz, which ensures weak coupling ($J \ll \nu_0$) between the qubits. For the initial state preparation, we initialize F_2 at infinite pseudospin temperature, $(\beta_2 h)^{-1} = \infty$ [43]. This is achieved by applying a $\pi/2$ pulse on F_2 followed by a PFG. For F_1, we prepare the qubit at different pseudospin temperatures by applying RF pulses from 0 to $\pi/2$, followed by a PFG. We then measure $\chi_\tau(u)$ by allowing heat exchange between F_1 and F_2 for a time duration $\tau = \pi/J$, corresponding to the maximum average heat exchange between the two qubits.

In Figs. 3(a) and 3(b) we display both experimental and theoretical results for the real and imaginary components of the CF $\chi_\tau(u)$ when F_1 is at a particular pseudospin temperature $(\beta_1 h)^{-1} = 1403$ Hz. We take a set of measurements in one complete period of $u \in [0, \frac{2\pi}{h\nu_0}]$ [red dots in Figs. 3(a) and 3(b)] and further take advantage of the periodicity of the CF, $\chi_\tau(u) = \chi_\tau(u + \frac{2\pi}{h\nu_0})$, to extrapolate [orange dots in Figs. 3(a) and 3(b)] the obtained data for subsequent periods. We phenomenologically add a small constant damping factor to $\chi_\tau(u)$ with a decay constant of 10 Hz in both theoretical and experimental data. The inverse Fourier transform of the obtained CF produces the desired PDF $p_\tau(Q)$, which shows three distinct peaks, at $Q/h = \pm 1$ kHz and $Q/h = 0$ Hz, and with finite widths proportional to the decay constant. The corresponding peak amplitudes reflect the probability of heat flowing from one qubit to another. The location of the peaks can be understood from the energy eigenvalues of the composite Hamiltonian $\mathcal{H}$ [Eq. (6)]. The ± 1 kHz peaks correspond to the transition between the zero-energy states and the highest- or lowest-energy states. The corresponding probabilities are proportional to $\frac{1}{2}\sin^2(\frac{J\tau}{2}) \times 1/(\exp(\mp\beta_1 h\nu_0) + 1)$. The peak at $Q = 0$ represents no heat-exchange process between the qubits, and in this particular scenario, its peak amplitude is
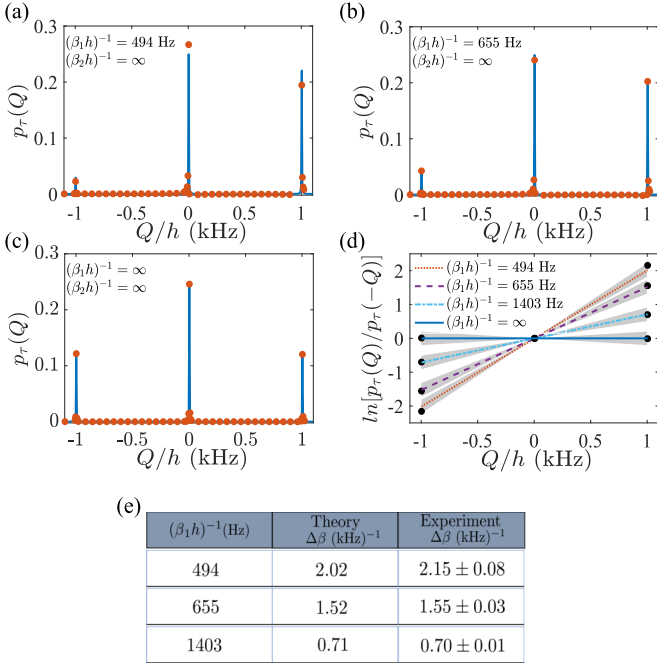
FIG. 4. (a–c) PDF of heat exchange for the *XY* model for different spin temperatures of F_1: (a) $(\beta_1 h)^{-1} = 494$ Hz, (b) $(\beta_1 h)^{-1} = 655$ Hz, and (c) $(\beta_1 h)^{-1} = \infty$. $(\beta_2 h)^{-1} = \infty$. Solid blue lines and red dots correspond to theoretical and experimental results, respectively. (d) Verification of Jarzynski and Wójcik heat XFT plots for $\ln[p_\tau(Q)/p_\tau(-Q)]$ as a function of Q/h for four F_1 temperatures. Shaded regions indicate the simulated 5% pulse errors in the experiment. (e) Table listing theoretical and experimentally obtained values for the slope $\Delta\beta = \beta_1 - \beta_2$, $\beta_i = 1/k_B T_i$ from (d). All other parameters are the same as in Fig. 3.

independent of the pseudospin temperatures and is proportional to $\frac{1}{2}(1 + \cos^2(\frac{J\tau}{2}))$. Note that, as per our convention, a positive value of Q corresponds to heat flowing from F_2 to F_1, and vice versa. Figure 3(c) therefore confirms that on average heat flows from hot qubit F_2 to cold qubit F_1 and thereby validates the second law of thermodynamics at the level of the ensemble average. However, in the microscopic realm, a finite probability corresponding to heat flowing from cold to hot exists which contributes to negative entropy production. With a reduction in the pseudospin temperature $(\beta_1 h)^{-1}$ the peak value at $Q/h = -1$ kHz decreases and, finally, disappears completely for $(\beta_1 h)^{-1} = 0$ [Fig. 3(d)].

In contrast, as the temperature of F_1 increases [Figs. 4(a)–4(c)] the probability of backflow of heat from F_1 to F_2 increases, and the peak value at $Q/h = -1$ kHz increases, becoming exactly equal to the peak value at $Q/h = 1$ kHz at $(\beta_1 h)^{-1} = \infty$ and thus ensuring zero net heat exchange at equilibrium. We next plot the ratio $\ln[p_\tau(Q)/p_\tau(-Q]$ against Q for four sets of pseudospin temperatures to confirm the Jarzynski and Wójcik XFT. Note that, as the coupling Hamiltonian in Eq. (6) is a constant one, $p_\tau(-Q)$ is obtained simply by flipping the forward PDF $p_\tau(Q)$. Figure 4(d) shows excellent agreement between the theoretical and the experimentally obtained results, with the expected slope equal to $\Delta\beta = \beta_1 - \beta_2$. The shaded regions indicate simulated results that involve 5% random errors in all the RF pulses used in

the interferometric technique as well as in the initial state preparation. In Fig. 4(e) we tabulate both theoretical and experimentally extracted values of these slopes.

It is experimentally possible to further tune the coupling J to explore the heat statistics and the corresponding XFT from the moderate- to the strong-coupling regime. However, interestingly for this particular model, the XFT is satisfied for arbitrary coupling strength J. This is due to the energy-preserving interaction term in the Hamiltonian [Eq. (6)] $H_{12} = \frac{hJ}{4}(\sigma_1^x \otimes \sigma_2^y - \sigma_1^y \otimes \sigma_2^x)$, which commutes with the total bare Hamiltonian of the two qubits $H_1 + H_2$. This symmetry implies for the energy change of the qubits, $\Delta E_1 = -\Delta E_2$ for any J value, as there is no energy cost involved in turning on or off the interaction between the two qubits. As a consequence, the XFT for heat exchange is supposed to be valid for any J value. We now present the proof by providing the exact analytical expression for the CF and the corresponding PDF $p_\tau(Q)$.

Following Eq. (4) and the Hamiltonian in Eq. (6), we perform simple algebraic manipulations of the Pauli matrices to receive an exact expression for $\chi_\tau(u)$ as

$$\chi_\tau(u) = \left[1 + \sin^2\left(\frac{J\tau}{2}\right)\{f_1(\nu_0)(1 - f_2(\nu_0))(e^{ihu\nu_0} - 1) \right.$$
$$\left. + f_2(\nu_0)(1 - f_1(\nu_0))(e^{-ihu\nu_0} - 1)\} \right], \quad (8)$$

where the function $f_i(\nu_0) = 1/(\exp(\beta_i h\nu_0) + 1)$, $i = 1, 2$, is evaluated at the inverse temperature β_i and qubit frequency ν_0. Note that the CF has the periodicity $\chi_\tau(u) = \chi_\tau(u + \frac{2\pi}{h\nu_0})$. Furthermore, as pointed out before, the above $\chi_\tau(u)$ follows the fluctuation symmetry $\chi_\tau(u) = \chi_\tau(-u + i\Delta\beta)$ for arbitrary coupling strength J as well as for arbitrary values of β_1, β_2, and ν_0.

The corresponding probability distribution function of heat $p_\tau(Q)$ can be simply extracted by performing the inverse Fourier transformation of $\chi_\tau(u)$,

$$p_\tau(Q) = \int_{-\infty}^{\infty} du\, e^{iuQ}\, \chi_\tau(u)$$
$$= p_{0,\tau}\delta(Q) + p_{+,\tau}\delta(Q - h\nu_0) + p_{-,\tau}\delta(Q + h\nu_0). \quad (9)$$

This expression clearly shows three distinct peaks for $p_\tau(Q)$ at $Q/h = 0, \pm\nu_0$, reflecting different heat-exchange processes between the qubits. These results excellently corroborate with our experimental plots as displayed in Figs. 3 and 4. In Eq. (9), $p_{+,\tau}$ and $p_{-,\tau}$ correspond to the probability of heat absorbed and heat released by qubit F_1, respectively, and are obtained from $\chi_\tau(u)$ as

$$p_{+,\tau} = \sin^2\left(\frac{J\tau}{2}\right)f_2(\nu_0)(1 - f_1(\nu_0)),$$
$$p_{-,\tau} = \sin^2\left(\frac{J\tau}{2}\right)f_1(\nu_0)(1 - f_2(\nu_0)), \quad (10)$$

and $p_{0,\tau} = 1 - p_{+,\tau} - p_{-,\tau} = 1 - \sin^2(\frac{J\tau}{2})(f_1(\nu_0) + f_2(\nu_0) - 2f_1(\nu_0)f_2(\nu_0))$ corresponds to the probability of no heat exchange between the qubits. It is easy to check that $p_{+,\tau}$ and $p_{-,\tau}$ are related via the fluctuation symmetry $p_{+,\tau} = e^{(\beta_1 - \beta_2)h\nu_0}p_{-,\tau}$. To further connect these analytical results to our experimental findings, in the limit where $(\beta_2 h)^{-1} = \infty$
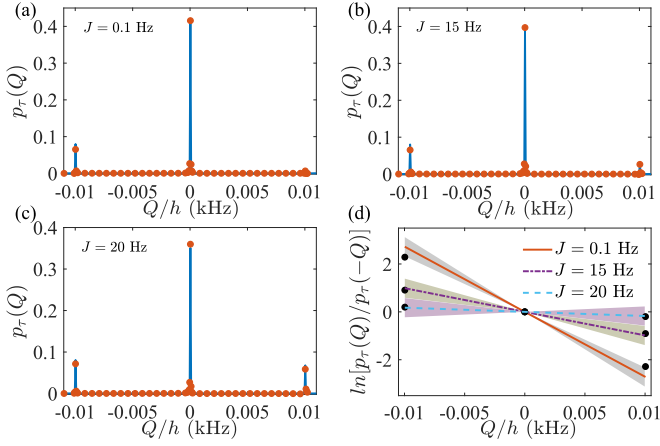
FIG. 5. (a–c) PDF of heat exchange for the *XX* model for $\nu_0 = 10$ Hz and for three values of coupling strength, J. The temperatures are fixed at $(\beta_1 h)^{-1} = 1403$ Hz and $(\beta_2 h)^{-1} = 288$ Hz. (a) $J = 0.1$ Hz (weak coupling), (b) $J = 15$ Hz (moderate coupling), and (c) $J = 20$ Hz (strong coupling). Solid blue lines and dots correspond to theoretical and experimental results, respectively. (d) Plots of $\ln[p_\tau(Q)/p_\tau(-Q)]$ as a function of Q for different coupling strengths. Shaded regions indicate simulated 5% pulse errors in the experiments.

and $(\beta_1 h)^{-1} = 0$, one finds following Eq. (10) that $p_{-,\tau}$ vanishes, which indicates no backflow of heat from F_1 to F_2. This outcome is confirmed in Fig. 3(d) as the absence of the peak at $Q/h = -\nu_0$. With increasing $(\beta_1 h)^{-1}$, the probability of backflow increases, and finally, at equilibrium ($\beta_1 = \beta_2$) the forward and backward flows become identical ($p_{-,\tau} = p_{+,\tau}$), confirming zero net heat exchange between the qubits. These predictions are also reflected in Figs. 4(a)–4(c).

In what follows, we experimentally emulate the *XX* model, which lacks the energy preserving symmetry between the qubits and investigate its consequence on heat statistics and the corresponding XFT.

B. *XX*-coupling model

We first display the experimental results for the *XX* model in Fig. 5. As before, we follow a similar experimental approach and set the frequency of the qubits to $\nu_0 = 10$ Hz but now tune J from 0.1 Hz up to 20 Hz to simulate $p_\tau(Q)$ from the weak- to the strong-coupling regime. We fix the temperatures for the qubits at $(\beta_1 h)^{-1} = 1403$ Hz and $(\beta_2 h)^{-1} = 288$ Hz and obtain the $p_\tau(Q)$ corresponding to a fixed time duration $\tau = \pi/J$. The PDFs $p_\tau(Q)$ for different values of J are shown in Figs. 5(a)–5(c). The trend for the distribution is similar to the earlier case, with three distinct peaks, at $Q = 0$, and $Q/h = \pm\nu_0$. However, the corresponding plot for the ratio $\ln[p_\tau(Q)/p_\tau(-Q)]$ versus Q in Fig. 5(d) shows a clear violation of the XFT, except for the value of $J = 0.1$ Hz. For $J = 0.1$ Hz $\ll \nu_0 = 10$ Hz (weak coupling) the obtained slope from the experimental data (black dots) matches very closely to the expected $\Delta\beta$ value (solid line). However, for moderate ($J = 15$ Hz) to strong coupling ($J = 20$ Hz), the experimental results (black dots) deviate significantly from the theoretical $\Delta\beta$ value (solid line), which is a clear indication of

the breakdown of the standard XFT. This breakdown can be attributed to the energy nonconserving coupling term in the *XX* model, as we show below.

To verify the XFT for this model, one can follow an approach similar to that for the *XY* model to obtain an analytical expression for the CF $\chi_\tau(u)$ However, instead of the CF, we provide here an expression for the deviation term of the XFT, i.e., $\langle e^{-\Delta\beta Q}\rangle_\tau - 1$, which captures the essential details about the violation. We obtain

$$\langle e^{-\Delta\beta Q}\rangle_\tau - 1 = -\frac{J^2}{J^2 + 16\,\nu_0^2}\sin^2\left(\frac{\tau}{4}\sqrt{J^2 + 16\,\nu_0^2}\right)$$
$$\times\, h(\beta_1, \beta_2, \nu_0), \tag{11}$$

where the function $h(\beta_1, \beta_2, \nu_0)$ is defined as

$$h(\beta_1, \beta_2, \nu_0) = \frac{1 + e^{\beta_1 h\nu_0} - e^{\beta_2 h\nu_0} - e^{(\beta_1 - \beta_2)h\nu_0}}{(e^{\beta_1 h\nu_0} + 1)}. \tag{12}$$

Note that the standard version of the XFT implies $\langle e^{-\Delta\beta Q}\rangle_\tau = 1$. The additional contribution in Eq. (11) therefore reflects the deviation from the XFT. This term yields a negligible contribution only in the weak-coupling limit $J \ll \nu_0$, which then reproduces the XFT for arbitrary τ. However, from moderate ($J \approx \nu_0$) to strong ($J \gg \nu_0$) coupling this term dominates, leading to the breakdown of the XFT as also observed experimentally. Note that this deviation term is in fact related to the total change in energy of the two qubits and, thereby, linked to the energy nonconserving coupling term $H_{12} = \frac{hJ}{4}\sigma_1^x \otimes \sigma_2^x$. We obtain

$$\langle\Delta E_1\rangle_\tau + \langle\Delta E_2\rangle_\tau = \frac{i}{h}\int_0^\tau dt\,\langle[H_{12}, H_1 + H_2]\rangle$$
$$= h\nu_0\frac{J^2}{J^2 + 16\,\nu_0^2}\sin^2\left(\frac{\tau}{4}\sqrt{J^2 + 16\,\nu_0^2}\right)$$
$$\times\, g(\beta_1, \beta_2, \nu_0), \tag{13}$$

where $\langle\Delta E_i\rangle_\tau$ is the net energy change of the ith qubit in the time duration τ and the function $g(\beta_1, \beta_2, \nu_0)$ is given as

$$g(\beta_1, \beta_2, \nu_0) = \frac{2\,(e^{(\beta_1 + \beta_2)h\nu_0} - 1)}{(e^{\beta_1 h\nu_0} + 1)\,(e^{\beta_2 h\nu_0} + 1)}. \tag{14}$$

Comparison of Eq. (11) and Eq. (13) clearly shows the link between the energy nonconserving interaction and the deviation of the XFT.

V. EFFECT OF THE INITIALLY CORRELATED STATE

We next direct our attention to exploring heat statistics for the correlated initial state. As mentioned earlier, the ancilla-based technique captures the effect of the arbitrary initial correlation present in the composite system (see Appendix A). Note that in the presence of such initial correlations the inverse FT of $\chi_\tau(u)$ may not correspond to the actual PDF of heat [44,45]. However, it produces the correct definition for the first cumulant, the average heat [46] $\langle Q\rangle = \text{Tr}_1[H_1(\rho_1(t) - \rho_1(0))]$, where $\rho_1(\tau)$ is the reduced density matrix of F_1 at time τ. In our experiment, we simulate the *XY* model, choose a particular uncorrelated initial state, introduce a finite amount
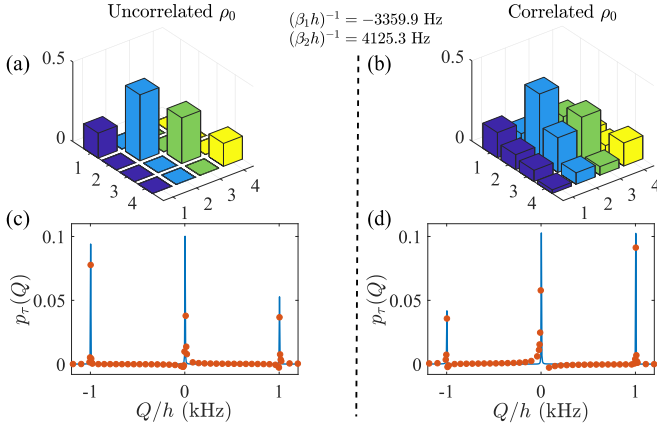
FIG. 6. Absolute values for the density matrix elements for the composite system F_1 and F_2 for the *XY* model for (a) uncorrelated ($\rho_0 = \rho_1 \otimes \rho_2$) and (b) correlated ($\rho_0 \neq \rho_1 \otimes \rho_2$) initial states. (c, d) Comparison between the corresponding heat-exchange PDFs $p_\tau(Q)$. Solid blue lines and dots represent theoretical and experimental results, respectively. Here the pseudospin temperatures for F_1 and F_2 are $(\beta_1 h)^{-1} = -3359.9\,\text{Hz}$ and $(\beta_2 h)^{-1} = 4125.3\,\text{Hz}$, respectively.

of correlation, affecting only the off-diagonal elements of the composite density matrix as shown in Figs. 6(a) and 6(b), and measure $\chi_\tau(u)$ to extract the corresponding $p_\tau(Q)$. In Figs. 6(c) and 6(d) we compare the distributions obtained for the correlated case versus the corresponding uncorrelated one. As shown, the presence of a finite correlation leads to a crucial change in the statistics and provides evidence of reversal of heat flow. This further implies the breakdown of the standard Jarzynski-Wójcik XFT. A similar effect for average heat flow has recently been studied experimentally for a two-qubit system by measuring the qubit states following quantum state tomography [46].

VI. SUMMARY

In summary, we experimentally explore the validity of the quantum version of the transient heat XFT by implementing an interferometric approach in a three-qubit liquid NMR architecture. We experimentally simulate two heat-exchange models. The experimental results show perfect agreement with the fluctuation symmetry when the composite system is weakly coupled and is prepared in the uncorrelated Gibbs thermal states with different temperatures. Interestingly, the *XY* model satisfies the XFT for arbitrary coupling strength, whereas for the *XX* model we observe the breakdown of the XFT in the strong-coupling regime. Furthermore, inclusion of any finite amount of correlation in the initial state also leads to a breakdown of the fluctuation symmetry and, interestingly, reverses the direction of the heat flow against the temperature bias, thereby providing an additional knob for controlling heat flow. We provide analytical results for these models and find excellent agreement with experiments. Future work will be directed towards implementing a quantum state tomography technique to monitor the qubit states to further analyze and test the relation between the heat exchange and Rényi divergences [47].
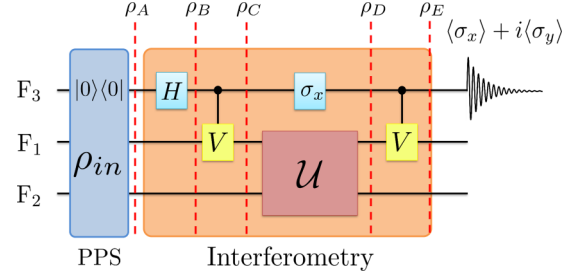

FIG. 7. Circuit diagram for the interferometric technique to measure the CF of heat $\chi_\tau(u)$. ρ_i ($i = A, B, C, D, E$) represents the intermediate states of the global system (F_1, F_2, F_3) after gate operations. $|0\rangle\langle 0|$ is the pseudopure state of the ancilla and ρ_{in} is an arbitrary initial state (correlated or uncorrelated) for the two qubits.

APPENDIX A: INTERFEROMETRIC TECHNIQUE TO OBTAIN THE CHARACTERISTIC FUNCTION FOR HEAT

In this section, we summarize the interferometric technique [23–25] to obtain the CF for heat as given in Eq. (4) in the text. We follow the circuit in Fig. 7. We begin with the initial state of the three-qubit system $|0\rangle\langle 0| \otimes \rho_{\text{in}}$, where ρ_{in} is an arbitrary initial state for the two qubits (F_1, F_2) that exchange heat and $|0\rangle\langle 0|$ is the state for the ancillary qubit. Therefore, the global density operator in the ancillary basis is given as

$$\rho_A = \begin{bmatrix} \rho_{\text{in}} & 0 \\ 0 & 0 \end{bmatrix}.$$

In the next step we apply the Hadamard gate, H, on the ancillary qubit. As a result, the density matrix is modified to

$$\rho_B = H \rho_A H^\dagger = \frac{1}{2} \begin{bmatrix} \rho_{\text{in}} & \rho_{\text{in}} \\ \rho_{\text{in}} & \rho_{\text{in}} \end{bmatrix}.$$

This operation is followed by application of a controlled gate $V = \exp[-i\,u\,H_1] \otimes 1_2$ on the qubit F_1. The corresponding change in the density matrix is given as

$$\rho_C = \frac{1}{2} \begin{bmatrix} \rho_{\text{in}} & \rho_{\text{in}} V^\dagger \\ V \rho_{\text{in}} & V \rho_{\text{in}} V^\dagger \end{bmatrix}.$$

The next step includes the unitary propagator $\mathcal{U}$ corresponding to the composite Hamiltonian $\mathcal{H}$ [Eq. (6)], along with a σ_x rotation on the ancillary qubit. The modified density matrix is given as

$$\rho_D = \frac{1}{2} \begin{bmatrix} \mathcal{U} V \rho_{\text{in}} V^\dagger \mathcal{U}^\dagger & \mathcal{U} V \rho_{\text{in}} \mathcal{U}^\dagger \\ \mathcal{U} \rho_{\text{in}} V^\dagger \mathcal{U}^\dagger & \mathcal{U} \rho_{\text{in}} \mathcal{U}^\dagger \end{bmatrix}.$$
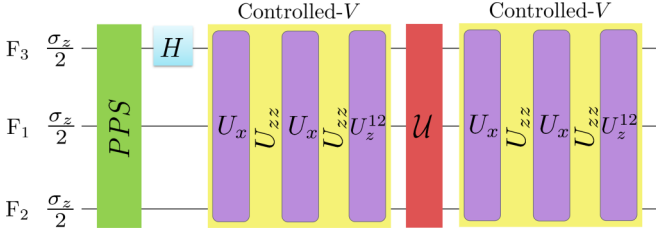
FIG. 8. Pulse sequence for the interferometric circuit in Fig. 7.

In the final step, the controlled gate V_1 is applied once again on qubit F_1. The final global density matrix is given by

$$\rho_E = \frac{1}{2}\begin{bmatrix} UV\rho_{in}V^\dagger\mathcal{U}^\dagger & UV\rho_{in}\mathcal{U}^\dagger V^\dagger \\ V\mathcal{U}\rho_{in}V^\dagger\mathcal{U}^\dagger & V\mathcal{U}\rho_{in}\mathcal{U}^\dagger V^\dagger \end{bmatrix}.$$

Now, tracing out qubits F_1 and F_2, we receive the reduced density matrix for the ancilla F_3 as

$$\rho = \text{Tr}_{1,2}[\rho_E] = \frac{1}{2}\begin{bmatrix} 1 & \text{Tr}[\mathcal{U}V\rho_{in}\mathcal{U}^\dagger V^\dagger] \\ \text{Tr}[V\mathcal{U}\rho_{in}V^\dagger\mathcal{U}^\dagger] & 1 \end{bmatrix}.$$

The off-diagonal components of this density matrix are simply related to the expectation values of the σ_x and σ_y components for the ancilla. We can therefore write

$$\begin{aligned}\langle\sigma_x\rangle_\rho + i\langle\sigma_y\rangle_\rho &= \text{Tr}[V\mathcal{U}\rho_{in}V^\dagger\mathcal{U}^\dagger], \\ &= \text{Tr}[V^\dagger\mathcal{U}^\dagger V\mathcal{U}\rho_{in}] \\ &= \text{Tr}[(e^{iuH_1}\otimes 1_2)\mathcal{U}^\dagger(e^{-iuH_1}\otimes 1_2)\mathcal{U}\rho_{in}] \\ &= \text{Tr}[\mathcal{U}^\dagger(e^{-iuH_1}\otimes 1_2)\mathcal{U}\rho_{in}(e^{iuH_1}\otimes 1_2)].\end{aligned}$$
$$(A1)$$

Note that the above final expression, Eq. (A1), is not yet the CF of heat as obtained in Eq. (4), following the two-time measurement protocol. It is only when the initial state ρ_{in} for F_1 and F_2 is given by an uncorrelated (product) Gibbs state, i.e., $\rho_{in} = \rho_0 = \exp[-\beta_1 H_1]/Z_1 \otimes \exp[-\beta_2 H_2]/Z_2$, which implies $[\rho_0, H_1\otimes 1_2] = 0$, that the above expression reduces to

$$\langle\sigma_x\rangle_\rho + i\langle\sigma_y\rangle_\rho = \text{Tr}[\mathcal{U}^\dagger(e^{-iuH_1}\otimes 1_2)\mathcal{U}(e^{iuH_1}\otimes 1_2)\rho_0],$$
$$(A2)$$

which is exactly the CF $\chi_\tau(u)$ in Eq. (4).

It is important to note that for an arbitrary initial condition Eq. (A1) may not deliver the correct PDF of heat, as it is not guaranteed to be always positive definite. However, interestingly, the CF at least produces the correct definition for the first moment, i.e., the average heat, given by $\langle Q\rangle = \text{Tr}_1[H_1(\rho_1(t) - \rho_1(0))]$.

APPENDIX B: PULSE SEQUENCE FOR THE INTERFEROMETRIC CIRCUIT FOR THE *XY* AND *XX* MODELS

The various gates used in the interferometric circuit, as shown in Fig. 7 (Fig. 2 in the text) are obtained by implementing the pulse sequence, shown in Fig. 8. In what follows, we explain Fig. 8: Each bordered box consists of three qubit
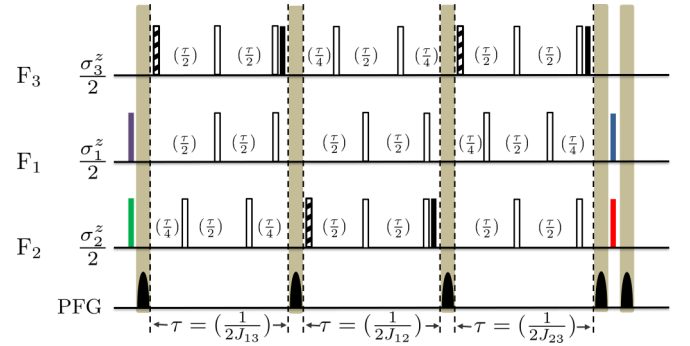

FIG. 9. NMR pulse sequence to prepare the initial state $|0\rangle\langle 0| \otimes \rho_1 \otimes \rho_2$. Filled black bars, dashed black bars, and open bars represent $(\frac{\pi}{4})_{-y}$, $(\frac{\pi}{4})_x$, and $(\pi)_x$ pulses, respectively. Green and purple bars represent $(\frac{\pi}{3})_x$ and $(0.42\pi)_x$ pulses. Blue and red bars control the temperature of F_1 and F_2, respectively. The PFG line shows the times at which gradients are applied to destroy the coherence.

pulses obtained using the GRAPE optimization technique [48]. The three-qubit liquid NMR system is found in the thermal equilibrium state at room temperature, the deviation density matrix of which can be written as $(\sigma_1^z + \sigma_2^z + \sigma_3^z)/2$. To prepare the uncorrelated initial state of $|0\rangle\langle 0| \otimes \rho_1 \otimes \rho_2$, where $\rho_i = \exp[-\beta_i H_i]/Z_i$, with Z_i being the respective partition function, we follow a pulse sequence similar to that shown in Fig. 9 [49]. After initialization, the Hadamard gate is implemented using GRAPE with a duration of 600 μs and fidelity of 99.9%. The control operation V can be split into z and x rotations and a free evolution under the $\sigma_i^z\sigma_j^z$ coupling, written as

$$V = \exp[-iuH_1] \otimes 1_2 = U_z^{12}U_{zz}U_xU_{zz}U_x, \quad (B1)$$

where $U_z^{12} = \exp[i\frac{\phi}{4}(\sigma_1^z + \sigma_2^z)]$, $U_{zz} = \exp[-i\frac{\phi}{8}(\sigma_1^z\sigma_2^z)]$, and $U_x = \exp[-i\frac{\pi}{2}(\sigma_1^x + \sigma_2^x)]$. ϕ is the angle of rotation and is expressed as $h\nu_0 u$. U_z^{12} and U_x are realized by using GRAPE, with the total maximum duration being 720 and 660 μs, respectively, with all fidelities being above 99.9%. U_{zz}, on the other hand, can be implemented by free evolution under the internal Hamiltonian of the molecule Eq. (5). The interaction operator $\mathcal{U}$ for the *XY* and *XX* models was again prepared using GRAPE, with a total time of 7.5 ms and a fidelity well over 99%.

APPENDIX C: INTERNAL HAMILTONIAN OF THE LIQUID NMR SYSTEM

In this section, we explain the internal Hamiltonian of the liquid NMR system given in Eq. (5) in the text. The NMR sample consists of 10^{15} molecules of 1,1,2-trifluoro-2-iodoethane (TFIE) dissolved in suitable solvents, acetone in our case, and placed in an external magnetic field directed along z, $\mathbf{B} = B_0\hat{z}$. This results in a Zeeman splitting term $\gamma_i\mathbf{B} \cdot \frac{\sigma_i}{2}$, where γ_i is the gyromagnetic ratio of the ith nucleus. Another Zaaman-like term, $\gamma_i \sum_{\mu,\nu} B_\mu d_{\mu\nu}^i \frac{\sigma_i^\nu}{2}$, arises because of the modifications of the electronic cloud surrounding the nucleus, where $d_{\mu\nu}^i$ is called the chemical shift tensor. The spins in the molecule can interact via a scalar J coupling, mediated by the electronic cloud through bonds and dipolar-

dipolar interaction, through space. As mentioned earlier, our liquid sample is diluted enough that intermolecular interactions can be neglected. Thus the Hamiltonian of the system takes the form

$$
H = \sum_i \gamma_i B_0 \left(\frac{\sigma_i^z}{2} + \sum_\nu d_{z\nu}^i \frac{\sigma_i^\nu}{2} \right) + \sum_{i<j,\mu,\nu} \frac{\sigma_i^\mu}{2} J_{ij}^{\mu\nu} \frac{\sigma_j^\nu}{2} + H_{\text{dipole}}. \quad \text{(C1)}
$$

Being prepared in the liquid state, the molecules in the sample undergo rapid rotations. The rotational motion averages out the dipole-dipole interaction and the electron-mediated spin-spin scalar coupling is averaged to its isotropic

value. The Hamiltonian thus reduces to

$$
H = \sum_{\mu,i=1}^N \gamma_i B_0 \left(\delta_{z\mu} + \bar{d}_{z\mu}^i \right) \frac{\sigma_i^\mu}{2} + \sum_{i<j=1}^N J_{ij} \frac{\boldsymbol{\sigma}_i}{2} \cdot \frac{\boldsymbol{\sigma}_j}{2}, \quad \text{(C2)}
$$

where J is the trace of the $J_{\mu\nu}$ tensor and $\bar{d}$ is a motionally averaged value of the chemical shift d tensor. N refers to the number of nuclei in a molecule. We recognize that $\omega_i = \gamma_i B_0 (1 + \bar{d}_{zz}^i)$ as the Larmor frequency of the ith nucleus in the system corresponds to the large external magnetic field B_0. For fluorine ($\gamma_i \sim 2.5 \times 10^8 \text{ s}^{-1} \text{ T}^{-1}$) this is of the order of 470 MHz at $B_0 = 11.74$ T. Further using secular approximation [50], the Hamiltonian simplifies to

$$
H = \sum_{i=1}^N \frac{h\nu_i}{2} \sigma_i^z + \sum_{i<j=1}^N \frac{h J_{ij}}{4} \sigma_i^z \sigma_j^z. \quad \text{(C3)}
$$

[1] C. Bustamante, J. Liphardt, and F. Ritort, The nonequilibrium thermodynamics of small systems, Phys. Today **58**(7), 43 (2005).

[2] G. Gallavotti and E. G. D. Cohen, Dynamical Ensembles in Nonequilibrium Statistical Mechanics, Phys. Rev. Lett. **74**, 2694 (1995).

[3] D. J. Evans, E. G. D. Cohen, and G. P. Morriss, Probability of Second Law Violations in Shearing Steady States, Phys. Rev. Lett. **71**, 2401 (1993).

[4] D. J. Evans and D. J. Searles, Equilibrium microstates which generate second law violating steady states, Phys. Rev. E **50**, 1645 (1994).

[5] C. Jarzynski, Nonequilibrium Equality for Free Energy Differences, Phys. Rev. Lett. **78**, 2690 (1997).

[6] G. E. Crooks, Entropy production fluctuation theorem and the nonequilibrium work relation for free energy differences, Phys. Rev. E **60**, 2721 (1999).

[7] C. Jarzynski and D. K. Wójcik, Classical and Quantum Fluctuation Theorems for Heat Exchange, Phys. Rev. Lett. **92**, 230602 (2004).

[8] U. Seifert, Entropy Production Along a Stochastic Trajectory and an Integral Fluctuation Theorem, Phys. Rev. Lett. **95**, 040602 (2005).

[9] D. J. Evans and D. J. Searles, The fluctuation theorem, Adv. Phys. **51**, 1529 (2002).

[10] S. R. Williams, D. J. Searles, and D. J. Evans, Nonequilibrium Free-Energy Relations for Thermal Changes, Phys. Rev. Lett. **100**, 250601 (2008).

[11] D. J. Evans, S. R. Williams, and D. J. Searles, A proof of Clausius' theorem for time reversible deterministic microscopic dynamics, J. Chem. Phys. **134**, 204113 (2011).

[12] M. Esposito, U. Harbola, and S. Mukamel, Nonequilibrium fluctuations, fluctuation theorems, and counting statistics in quantum systems, Rev. Mod. Phys. **81**, 1665 (2009).

[13] M. Campisi, P. Hänggi, and P. Talkner, *Colloquium:* Quantum fluctuation relations: Foundations and applications, Rev. Mod. Phys. **83**, 771 (2011).

[14] P. Hänggi and P. Talkner, The other QFT, Nat. Phys. **11**, 108 (2015).

[15] C. Jarzynski, Equalities and inequalities: Irreversibility and the second law of thermodynamics at the nanoscale, Annu. Rev. Condens. Matter Phys. **2**, 329 (2011).

[16] K. Saito and Y. Utsumi, Symmetry in full counting statistics, fluctuation theorem, and relations among nonlinear transport coefficients in the presence of a magnetic field, Phys. Rev. B **78**, 115429 (2008).

[17] D. Andrieux, P. Gaspard, T. Monnai, and S. Tasaki, The fluctuation theorem for currents in open quantum systems, New. J. Phys. **11**, 043014 (2009).

[18] U. Seifert, Stochastic thermodynamics, fluctuation theorems, and molecular machines, Rep. Prog. Phys. **75**, 126001 (2012).

[19] J. Millen and A. Xuereb, Perspective on quantum thermodynamics, New J. Phys. **18**, 011002 (2016).

[20] S. Vinjanampathy and J. Anders, Quantum thermodynamics, Contemp. Phys. **57**, 545 (2016).

[21] G. Katz and R. Kosloff, Quantum thermodynamics in strong coupling: Heat transport and refrigeration, Entropy **18**, 186 (2016).

[22] G. Huber, F. Schmidt-Kaler, S. Deffner, and E. Lutz, Employing Trapped Cold Ions to Verify the Quantum Jarzynski Equality, Phys. Rev. Lett. **101**, 070403 (2008).

[23] M. Campisi, R. Blattmann, S. Kohler, D. Zueco, and P. Hanggi, Employing circuit QED to measure non-equilibrium work fluctuations, New J. Phys. **15**, 105028 (2013).

[24] L. Mazzola, G. De Chiara, and M. Paternostro, Measuring the Characteristic Function of the Work Distribution, Phys. Rev. Lett. **110**, 230602 (2013).

[25] R. Dorner, S. R. Clark, L. Heaney, R. Fazio, J. Goold, and V. Vedral, Extracting Quantum Work Statistics and Fluctuation Theorems by Single-Qubit Interferometry, Phys. Rev. Lett. **110**, 230601 (2013).

[26] J. Goold, U. Poschinger, and K. Modi, Measuring the heat exchange of a quantum process, Phys. Rev. E **90**, 020101(R) (2014).

[27] J. P. S. Peterson, R. S. Sarthour, A. M. Souza, I. S. Oliveira, J. Goold, K. Modi, D. O. Soares-Pinto, and L. C. Céleri, Experimental demonstration of information to energy conversion in

a quantum system at the Landauer limit, Proc. R. Soc. A **472**, 20150813 (2016).

[28] J. P. S. Peterson, T. B. Batalhäo, M. Herrera, A. M. Souza, R. S. Sarthour, I. S. Oliveira, and R. M. Serra, Experimental characterization of a spin quantum heat engine, arXiv:1803.06021.

[29] T. B. Batalhão, A. M. Souza, L. Mazzola, R. Auccaise, R. S. Sarthour, I. S. Oliveira, J. Goold, G. De Chiara, M. Paternostro, and R. M. Serra, Experimental Reconstruction of Work Distribution and Study of Fluctuation Relations in a Closed Quantum System, Phys. Rev. Lett. **113**, 140601 (2014).

[30] S. An, J.-N. Zhang, M. Um, D. Lv, Y. Lu, J. Zhang, Z.-Q. Yin, H. T. Quan, and K. Kim, Experimental test of the quantum Jarzynski equality with a trapped-ion system, Nat. Phys. **11**, 193 (2015).

[31] T. P. Xiong, L. L. Yan, F. Zhou, K. Rehan, D. F. Liang, L. Chen, W. L. Yang, Z. H. Ma, M. Feng, and V. Vedral, Experimental Verification of a Jarzynski-Related Information-Theoretic Equality by a Single Trapped Ion, Phys. Rev. Lett. **120**, 010601 (2018).

[32] A. Smith, Y. Lu, S. An, X. Zhang, J. N. Zhang, Z. Gong, H. T. Quan, C. Jarzynski, and K. Kim, Verification of the quantum nonequilibrium work relation in the presence of decoherence, New J. Phys. **20**, 013008 (2018).

[33] M. Campisi, P. Talkner, and P. Hänggi, Influence of measurements on the statistics of work performed on a quantum system, Phys. Rev. E **83**, 041114 (2011).

[34] G. T. Landi and D. Karevski, Fluctuations of the heat exchanged between two quantum spin chains, Phys. Rev. E **93**, 032122 (2016).

[35] B. K. Agarwalla, B. Li, and J.-S. Wang, Full-counting statistics of heat transport in harmonic junctions: Transient, steady states, and fluctuation theorems, Phys. Rev. E **85**, 051142 (2012).

[36] K. Saito and A. Dhar, Fluctuation Theorem in Quantum Heat Conduction, Phys. Rev. Lett. **99**, 180601 (2007).

[37] B. K. Agarwalla, H. Li, B. Li, and J.-S. Wang, Exchange fluctuation theorem for heat transport between multiterminal harmonic systems, Phys. Rev. E **89**, 052101 (2014).

[38] T. Denzler and E. Lutz, Heat distribution of a quantum harmonic oscillator, Phys. Rev. E **98**, 052106 (2018).

[39] J. Cavanagh, W. J. Fairbrother, A. G. Palmer III, and N. J. Skelton, *Protein NMR Spectroscopy: Principles and Practice* (Elsevier, Amsterdam, 1995).

[40] M. H. Levitt, *Spin Dynamics: Basics of Nuclear Magnetic Resonance* (John Wiley and Sons, New York, 2001).

[41] J. Teles, E. R. DeAzevedo, J. C. C. Freitas, R. S. Sarthour, I. S. Oliveira, and T. J. Bonagamba, Quantum information processing by nuclear magnetic resonance on quadrupolar nuclei, Phil. Trans. R. Soc. A **370**, 4770 (2012).

[42] D. G. Cory, M. D. Price, and T. F. Havel, Nuclear magnetic resonance spectroscopy: An experimentally accessible paradigm for quantum computing, Physica D **120**, 82 (1998).

[43] A. Abragam and W. G. Proctor, Spin temperature, Phys. Rev. **109**, 1441 (1958).

[44] P. Solinas and S. Gasparinetti, Probing quantum interference effects in the work distribution, Phys. Rev. A **94**, 052103 (2016).

[45] M. Perarnau-Llobet, E. Bäumer, K. V. Hovhannisyan, M. Huber, and A. Acin, No-Go Theorem for the Characterization of Work Fluctuations in Coherent Quantum Systems, Phys. Rev. Lett. **118**, 070601 (2017).

[46] K. Micadei, J. P. S. Peterson, A. M. Souza, R. S. Sarthour, I. S. Oliveira, G. T. Landi, T. B. Batalhão, R. M. Serra, and E. Lutz, Reversing the direction of heat flow using quantum correlations, Nat. Commun. **10**, 2456 (2019).

[47] B.-B. Wei, Relations between heat exchange and Rényi divergences, Phys. Rev. E **97**, 042107 (2018).

[48] N. Khaneja *et al.*, Optimal control of coupled spin dynamics: design of NMR pulse sequences by gradient ascent algorithms, J. Magn. Reson. **172**, 296 (2005).

[49] H. Katiyar, A. Shukla, K. R. K. Rao, and T. S. Mahesh, Violation of entropic Leggett-Garg inequality in nuclear spins, Phys. Rev. A **87**, 052102 (2013).

[50] M. H. Levitt, *Spin Dynamics: Basics of Nuclear Magnetic Resonance* (John Wiley and Sons, New York, 2001).